https://doi.org/10.1016/j.optlaseng.2023.107957

Correspondence imaging through complex scattering media with temporal correction

Yin Xiao[a], Lina Zhou[a], Wen Chen[a,b,*]

[a]Department of Electrical and Electronic Engineering,
The Hong Kong Polytechnic University, Hong Kong, China
[b]Photonics Research Institute,
The Hong Kong Polytechnic University, Hong Kong, China
*Corresponding author. E-mail address: owen.chen@polyu.edu.hk

Abstract: Object reconstruction in optical imaging through complex scattering media is challenging. The existence of multiple and dynamic scatterings in complex environments leads to nonlinear reconstruction problem, inducing significant complexity in object reconstruction. In this paper, we report a correspondence imaging approach to reconstructing high-quality objects through complex scattering media where conventional methods cannot work. To complete formation mechanism of correspondence imaging through complex scattering media, a rectified theory is derived to implement object reconstruction. In the proposed method, temporal correction is introduced to eliminate the effect of dynamic scaling factors which physically exist in complex scattering environments. Then, a series of light intensities collected by a single-pixel bucket detector can be temporally corrected for the proposed correspondence imaging through complex scattering media. A series of optical experiments are conducted to show advantages of the proposed method over conventional methods in complex scattering environments. In addition, the proposed principle can be flexibly used with other methods to further enhance quality of the reconstructed objects. The proposed method provides a powerful tool to reconstruct high-quality objects through complex scattering media with single-pixel measurements, and the proposed method could provide an insight into correspondence imaging through complex scattering media.

Keywords: Correspondence imaging; Complex scattering media; Object reconstruction; Temporal correction

1. Introduction

Current imaging systems usually employ two-dimensional (2D) digital camera, e.g., a charge-coupled detector (CCD), to capture a snapshot image within an exposure period [1,2]. The optical imaging systems use physical approaches, and the imaging mechanism is to map a scene to a 2D sensor plane. However, when optical wave propagates through scattering media, a speckle pattern could be generated due to constructive and destructive interference. The light intensity variations in scattering environments could result in blurry images with low signal-to-noise ratio (SNR) [3]. Hence, imaging through scattering media has been a pervasive problem, and is fundamental in numerous applications, e.g., deep tissue imaging [4], wavefront shaping [5–7] and inverse problems [8–10]. In practice, there is an increasing demand for high-quality optical imaging through scattering media [11–13], and the limitations of optical imaging systems with 2D cameras in scattering environments could be apparent.

To address the challenges encountered in optical imaging, single-pixel imaging (e.g., correspondence imaging) has emerged as a promising and powerful tool in solving inverse problems [14–19]. In single-pixel imaging, sensor arrays used in conventional imaging systems are replaced by a single-pixel detector, and the trade-off is that a series of measurements are needed. The single-pixel imaging has several advantages. For instance, a single-pixel detector has high efficiency, and can detect weak light intensities [20]. In addition, a single-pixel detector has merits of low cost and high capability in the circumstances with non-visible wavelengths (e.g., X-ray [21–23] and terahertz [24–26]). The single-pixel imaging methods have transferred conventional imaging burden from high-quality hardware (e.g., lens quality, numerical aperture, density of the sensor array and pixel size) to the computations. In the single-pixel imaging, a series of illumination patterns are used to encode the features of a target into a number of single-pixel light intensities. The collected single-pixel light intensities are a one-dimensional (1D) signal, and different algorithms were developed to extract object information by using the collected 1D signal [27–40]. In various single-pixel imaging methods, it was found that correspondence imaging [33–40] can generate positive and negative images by conditionally averaging the series of

illumination patterns. The correspondence imaging provides a simple strategy for object reconstruction, and shows advantages in many aspects, e.g., storage space, memory consumption and computational time.

Although correspondence imaging has been demonstrated to be effective, there are still some limitations. Some research groups have conducted the studies to demonstrate effectiveness of imaging methods through scattering media [41–49]. However, conventional correspondence imaging mainly focuses on the study of its feasibility and characteristics in static scattering scenarios. In complex scattering environments (e.g., dynamic and turbid water), the existence of multiple and dynamic scattering leads to nonlinear reconstruction problems, inducing significant complexity in object reconstruction. In complex scattering environments, it could be impossible to accurately describe light propagation using mathematical tools. Therefore, it is a great challenge to realizing object reconstruction using correspondence imaging through complex scattering media. High-quality object reconstruction through complex scattering media shows a great significance in many applications, e.g., bioscience and autonomous navigation. Therefore, developing an effective algorithm to reconstruct object information through complex scattering media is significant and desirable.

In this paper, we report a correspondence imaging approach to extracting high-quality object information through complex scattering media where conventional methods cannot work. To complete the formation mechanism of correspondence imaging through complex scattering media, a rectified theory is derived to implement object reconstruction. In complex scattering environments, scaling factors physically existing in an optical channel are dynamically changed, and could significantly affect object reconstruction. In the proposed method, temporal correction is introduced to eliminate the effect of dynamic scaling factors which physically exist in optical channel. Then, light intensities collected by a single-pixel detector are temporally corrected for the developed correspondence imaging through complex scattering media. A series of experiments are conducted to illustrate advantages of the proposed method over conventional methods.

2. Model and theoretical derivations

2.1. Model

In single-pixel imaging or ghost imaging, a series of random illumination patterns $I_i(\mathbf{x})(i=1,2,3\ldots)$ sequentially illuminate an object $G(\mathbf{x})$ with spatial coordinate $\mathbf{x}$. After propagating through complex and dynamic scattering media, object wave is collected by a single-pixel bucket detector. This process is described in Fig. 1(a). In Fig. 1(a), I_{im} denotes the mth element of an illumination pattern I_i, and G_m denotes the mth element of the object G. The optical intensity just behind object is described by $A_i(\mathbf{x})$, which is equivalent to a dot product of $I_i(\mathbf{x})$ and $G(\mathbf{x})$. Here, A_{im} denotes the mth element of optical intensity $A_i(\mathbf{x})$. Then, the optical wave propagates through scattering media, and is collected by a single-pixel detector.

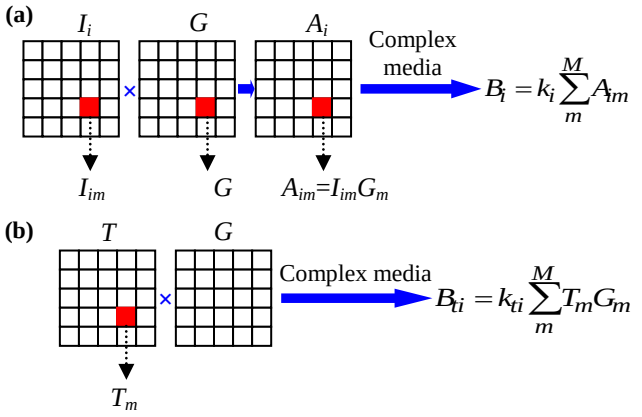

Fig. 1. (a) A schematic of single-pixel detection, and (b) a schematic of single-pixel detection with a temporally-corrected pattern.

The single-pixel detection process can be described by

$$B_i = k_i \sum_m^M A_{im} = k_i \sum_m^M I_{im} G_m, \tag{1}$$

where B_i denotes a single-pixel intensity value corresponding to the illumination pattern $I_i(\mathbf{x})$, M denotes the total number of pixels in the pattern, and k_i denotes a scaling factor existing in complex optical channel when the illumination pattern $I_i(\mathbf{x})$ is used. In static environments, when the detector is fixed, the scaling factor could be considered as a constant. In complex and dynamic scattering media, scaling factors are dynamically changed and determined by the optical channel. Therefore, it is necessary to eliminate the effect. Here, a temporally-corrected pattern $T(\mathbf{x})$ is introduced as shown in Fig. 1(b). In Fig. 1(b), T_m denotes the mth element of the pattern T. It is worth mentioning that $T(\mathbf{x})$ and $I_i(\mathbf{x})$ are alternately used to illuminate the object, and $T(\mathbf{x})$ is fixed in the whole measurement process. When temporally-corrected pattern is used to illuminate the object, single-pixel detection process can be described by

$$B_{ti} = k_{ti}\sum_{m}^{M} T_m G_m = \rho k_{ti}, \tag{2}$$

where B_{ti} denotes single-pixel intensities corresponding to the temporally-corrected pattern, k_{ti} denotes a scaling factor when the temporally-corrected pattern is applied, and ρ denotes a constant which is equal to $\sum T_m G_m$.

Since the temporally-corrected pattern is used just before each illumination pattern, it is feasible to assume that time interval between the temporally-corrected pattern and each corresponding illumination pattern is short. In this case, we can consider that scaling factor k_{ti} is equal to k_i. Combining Eqs. (1) and (2), we have

$$\sum_{m}^{M} I_{im} G_m = \rho \frac{B_i}{B_{ti}}. \tag{3}$$

Here, a new symbol B_i' is applied to replace the left part of Eq. (3), and then we have

$$B_i' = \rho \frac{B_i}{B_{ti}}, \tag{4}$$

where B_i' denotes effective single-pixel intensities obtained in complex and dynamic scattering environment which is able to effectively eliminate the effect of dynamic scaling factors.

It is worth noting that in the proposed method, the temporally-corrected pattern can be one randomly-generated amplitude-only pattern, and the temporally-corrected pattern has no relationship with the illumination patterns. Once the temporally-corrected pattern is chosen, it should be fixed. Then, the fixed temporally-corrected pattern and each illumination pattern are alternately used to sequentially illuminate a target. The fixed temporally-corrected pattern is used to eliminate effect of dynamically-generated scaling factors in the complex optical channel, and the fixed temporally-corrected pattern is not used in the final object reconstruction. Therefore, randomness of temporally-corrected pattern could have no effect on quality of reconstructed objects.

2.2. Gaussian distribution of single-pixel intensity sequence

In static scattering environments, the collected single-pixel intensities obey a Gaussian distribution, when a series of random illumination patterns sequentially illuminate an object. In a complex and dynamic scattering environment, it is different due to complex optical channel characteristics, i.e., dynamic scaling factors. When Gaussian distribution of single-pixel intensity sequence is severely destroyed in complex scattering environment, the object cannot be effectively reconstructed. In the proposed correspondence imaging, the introduced temporally-corrected pattern helps eliminate the effect of dynamic scaling factors in complex environments, and an effective single-pixel intensity sequence with Gaussian distribution can be generated when a series of random patterns are used to illuminate the object. Mathematically, the effective single-pixel intensity sequence obeys a Gaussian distribution, and probability density function is described by

$$f_{B_i'}(b_i') = \frac{1}{\sqrt{2\pi}\sigma'} e^{-(b_i'-\mu')/2\sigma'^2}, \tag{5}$$

where b_i' denotes a possible value that B_i' takes, $\mu' = \sum G_m E(I_i)$ denotes expectation of effective single-pixel intensity sequence, and $\sigma'^2 = \sum G_m^2 D(I_i)$ denotes a variance of effective single-pixel intensity sequence. $E(I_i)$ denotes expectation of the illumination pattern, and $D(I_i)$ denotes variance of the illumination pattern. Here, the value of μ' is usually not 0.5, and depends on the object. In the simulations and experiments, parameter μ' can be calculated by using the obtained effective single-pixel light intensities. Typical distributions of directly-collected intensity sequences and temporally-corrected intensity sequences are given in Sec. III.

2.3. Positive and negative imaging through complex scattering media

To explore formation mechanism of positive imaging through complex and dynamic scattering media, we calculate conditional expectation $E(I_{in}|b_i' \geq \mu')$ related to $E(A_{in}|b_i' \geq \mu')$. The conditional expectation $E(A_{in}|b_i' \geq \mu')$ is described by [39]

$$E(A_{in}|b_i' \geq \mu') = \frac{\int_{\mu'}^{\infty}\int_{0}^{b_i'} a_{in} f_{B_i'}(b_i') da_{in} db_i'}{\int_{\mu'}^{\infty} f_{B_i'}(b_i') db_i'}, \tag{6}$$

where A_{in} denotes an element of $A_i(\mathbf{x})$ to be studied, and a_{in} denotes a possible value that A_{in} takes. All other elements $A_{im}\ (m \neq n)$ in $A_i(\mathbf{x})$ are considered as a whole part, and then we have

$$B_i' = \sum_{m}^{M} I_{im} G_m = \sum_{m \neq n}^{M} I_{im} G_m + A_{in} = Q_i + A_{in}, \tag{7}$$

where

$$Q_i = \sum_{m \neq n}^{M} I_{im} G_m, \tag{8}$$

with a mean value of

$$\mu_Q = \sum_{m \neq n}^{M} G_m E(I_i), \tag{9}$$

and a variance of

$$\sigma_Q^2 = \sum_{m \neq n}^{M} G_m^2 D(I_i). \tag{10}$$

In Eq. (7), effective single-pixel intensity value B_i' is divided into two parts, i.e., Q_i and A_{in}. Q_i denotes the sum of all the elements except the elements A_{in} in the pattern A_i. It is worth noting that there is a noticeable difference in Eq. (7) between conventional method and the proposed correspondence imaging through complex scattering media. When conventional correspondence imaging is applied, we have

$$\begin{aligned} B_i &= k_i \sum_{m}^{M} I_{im} G_m \\ &= k_i \sum_{m \neq n}^{M} I_{im} G_m + k_i A_{in} \\ &= k_i Q_i + k_i A_{in}. \end{aligned} \tag{11}$$

Since k_i is related to characteristics of optical channel, it depends on wave propagation environments. A dynamic and scattering environment causes the variation of k_i. In this case, expectation μ and variance σ^2 of B_i are dynamically changed in complex scattering environments. As a result, calculating the expectation, i.e., $E(A_{in}|b_i \geq \mu)$, cannot effectively reconstruct the object due to dynamic scaling factors. In the proposed correspondence imaging, dynamic scaling factors are eliminated as illustrated in Eq. (4), so it is meaningful to calculate conditional expectation $E(A_{in}|b_i' \geq \mu')$ in order to reconstruct the test object.

Inspired by the work in Ref. [39], we can further get the expectation of $E(A_{in}|b_i' \geq \mu')$, which could be described by

$$E(A_{in}|b_i' \geq \mu') = E(A_{in}) + \frac{2}{\sqrt{2\pi}\sigma_Q} D(A_{in}). \tag{12}$$

In Eq. (12), the left part is related to formation mechanism of positive imaging through complex and dynamic scattering media, i.e., $E(I_{in}|b_i' \geq \mu')$. The relationship between $E(A_{in}|b_i' \geq \mu')$ and $E(I_{in}|b_i' \geq \mu')$ is described by

$$\begin{aligned} E(A_{in}|b_i' \geq \mu') &= E(I_{in} G_n | b_i' \geq \mu') \\ &= G_n E(I_{in}|b_i' \geq \mu'). \end{aligned} \tag{13}$$

The right part of Eq. (12) can be described by

$$\begin{aligned} &E(A_{in}) + \frac{2}{\sqrt{2\pi}\sigma_Q} D(A_{in}) \\ &= E(I_{in} G_n) + \frac{2}{\sqrt{2\pi}\sigma_Q} D(I_{in} G_n) \\ &= G_n E(I_{in}) + \frac{2}{\sqrt{2\pi}\sigma_Q} G_n^2 D(I_{in}). \end{aligned} \tag{14}$$

Combining Eqs. (12)–(14), we have

$$\begin{aligned} &E(I_{in}|b_i' \geq \mu') \\ &= E(I_{in}) + \frac{2}{\sqrt{2\pi}\sigma_Q} G_n D(I_{in}) \\ &= \alpha + \beta G_n, \end{aligned} \tag{15}$$

where $\alpha = E(I_{in})$ and $\beta = 2D(I_{in})/\sqrt{2\pi}\sigma_Q$.

Based on Eq. (15), it is straightforward to find that average values of the illumination patterns are proportional to the corresponding object in the case of $b_i' \geq \mu'$. Therefore, formation mechanism of positive imaging through complex scattering media is theoretically demonstrated.

In order to explore formation mechanism of negative imaging through complex scattering media, it is necessary to calculate conditional expectation $E(I_{in}|b_i' < \mu')$ which is related to $E(A_{in}|b_i' < \mu')$. Here, $E(A_{in}|b_i' < \mu')$ can be described by

$$E(A_{in}|b_i' < \mu') = \frac{\int_0^{\mu'} \int_0^{b'} a_{in} f_{B_i'}(b_i') da_{in} db_i'}{\int_0^{\mu'} f_{B_i'}(b_i') db_i'}. \tag{16}$$

Similar to theoretical description of positive imaging, we have

$$E(A_{in}|b_i' < \mu') = E(A_{in}) - \frac{2}{\sqrt{2\pi}\sigma_Q} D(A_{in}). \tag{17}$$

Based on Eq. (17), we have

$$E(I_{in}|b_i' < \mu') = \alpha - \beta G_n. \tag{18}$$

In Eq. (18), it is straightforward to find that average values of the illumination patterns are proportional to the corresponding object in the case of $b_i' < \mu'$. Hence, formation

mechanism of negative imaging through complex scattering media is also theoretically demonstrated.

2.4. Algorithm description

The proposed positive and negative imaging through complex scattering media is further illustrated in **Algorithm 1**. In **Algorithm 1**, χ denotes the number of illumination patterns identified for positive imaging through complex scattering media, and η denotes the number of illumination patterns identified for negative imaging through complex scattering media. *pos* denotes a recovered positive image, and *neg* denotes a recovered negative image. *cor* denotes a final correspondence image (i.e., *pos*–*neg*), and N denotes the total number of illumination patterns.

Algorithm 1: Temporal Correction and Reconstruction.

Input: $I_i(\mathbf{x})$, B_i, B_{ti},

1. Initialize: $\chi = 1$, $\eta = 1$, *pos* = 0, *neg* = 0, *cor* = 0
2. **for** *i* from 1 to *N* **do**
3. $B_i' = \frac{B_i}{B_{ti}}$
4. **end**
5. Calculate mean value of B_i', i.e., μ'
6. **for** *i* from 1 to *N* **do**
7. **if** $B_i' \geq \mu'$ **do**
8. $pos = \left[pos \times (\chi - 1) + I_i(\mathbf{x}) \right] / \chi$,
9. $\chi = \chi + 1$,
10. **else do**
11. $neg = \left[neg \times (\eta - 1) + I_i(\mathbf{x}) \right] / \eta$,
12. $\eta = \eta + 1$,
13. **end**
14. *cor* = *pos*–*neg*
15. **end**

Output: *pos*, *neg*, *cor*.

3. Experimental results and discussion

3.1. Experimental setup

A series of optical experiments are conducted to verify feasibility and effectiveness of the proposed correspondence imaging through complex and dynamic scattering media. A schematic of experimental setup is shown in Fig. 2.

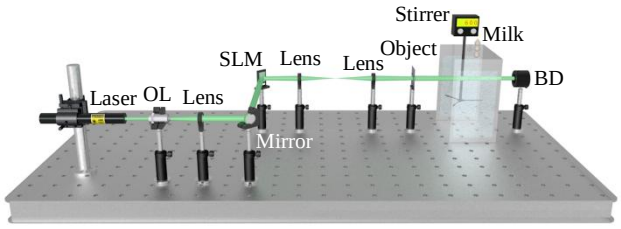

Fig. 2. A schematic of experimental setup in complex, dynamic and highly strong scattering media to verify the proposed correspondence imaging. OL: Objective lens; SLM: Spatial light modulator; BD: Single-pixel bucket detector.

In Fig. 2, a green laser with wavelength of 532.0 nm is used, and the maximum output power of the laser is 25.0 mW. A lens with a focal length of 100.0 mm collimates the laser after the laser is expanded by an objective lens. The collimated laser illuminates an amplitude-only SLM (Holoeye, LC-R720) with pixel size of 20.0 μm. A series of random amplitude-only patterns are sequentially embedded into the SLM, and are used to sequentially illuminate an object through a 4*f* lens system. Here, a fixed temporal carrier and a series of illumination patterns are alternately embedded into the amplitude-only SLM. Time interval between the temporally-corrected pattern and the illumination pattern is set as 80 ms. A dynamic water environment is created by using a stirrer with a speed of 600.0 rpm, and highly strong scattering is also caused by skimmed milk to be kept dropping into a water tank. In general, a low refresh rate could limit performance of the proposed method, and the higher refresh rate is highly desirable. The water tank is made of transparent polymethyl methacrylate, and has a dimension of 10.0 cm (L) × 30.0 cm (W) × 30.0 cm (H). At the beginning, the water tank holds 6000.0 ml of clean water, and during the imaging process 10.0 ml skimmed milk mixed with 500.0 ml clean water keeps dropping into the water tank over 107.0 minutes. In optical experiments, 40000 illumination patterns are applied, and the temporally-corrected pattern is repeatedly used for 40000 times. The total time for collecting all experimental data is about 107 minutes. At the receiving end, a series of light intensities are recorded by a single-pixel bucket detector (Thorlabs, PDA100A2). An axial distance is 22.0 cm between water tank and single-pixel detector, and an axial distance is 42.0 cm between the object and single-pixel detector in optical experiments. To quantify the scattering level of complex environment shown in Fig. 2, attenuation coefficient based on the Beer-Lambert law can be calculated [50–53]. The calculated attenuation coefficients demonstrate that the scattering level has an obvious change during the milk drop process

[52,53]. When there is an extra scattering medium between the SLM and the object, optical channel characteristic, i.e., scaling factors, is also changed. Since the introduced temporally-corrected pattern can eliminate the effect of scaling factors on object reconstruction in the proposed method, the extra scattering medium has no much effect on object reconstruction.

3.2. Resolution target

For a developed imaging system, it is crucial to test the resolution that can be achieved based on the experimental setup. Here, the first optical experiment is to test spatial resolution achieved by using the proposed correspondence imaging. In Fig. 2, a USAF 1951 resolution target serves as an object. It is well known that USAF 1951 resolution target consists of some groups, and each group contains several elements. The larger the group number and element number, the higher spatial resolution is. Then, temporally-corrected pattern and a series of illumination patterns are alternately applied to illuminate USAF 1951 resolution target, and object wave propagating through dynamic and turbid water is collected by a single-pixel bucket detector. The directly collected single-pixel intensities are shown in Fig. 3(a). As shown in Fig. 3(a), the directly collected single-pixel intensities decrease as the milk keeps dropping into the dynamic water tank. The single-pixel intensity values directly collected at the beginning and at the end have a big difference. Therefore, complex scattering media severely affect optical imaging process. When temporally-corrected patterns are applied, temporally-corrected intensities are shown in Fig. 3(b). The rectified distribution of single-pixel intensities can be observed, and it is demonstrated that the proposed method effectively eliminates effect of dynamic scaling factors in complex scattering environments. As discussed in Sec. II, probability distribution of the collected single-pixel intensities in single-pixel imaging obeys a Gaussian distribution. Without temporal correction, the directly collected single-pixel intensities do not satisfy the property of Gaussian distribution, as shown in Fig. 3(c). Using the proposed method, the corrected single-pixel intensities obey a nearly perfect Gaussian distribution, as shown in Fig. 3(d). In Figs. 3(c) and 3(d), ΔB denotes the difference between the directly collected single-pixel intensities and a mean value of the directly collected single-pixel intensities, and $\Delta B'$ denotes the difference between temporally-collected single-pixel intensities and a mean value of temporally-collected single-pixel intensities. The negative and positive legends in Figs. 3(c) and 3(d) mean that the corresponding single-pixel intensities can be applied to further identify the illumination patterns for retrieving negative and positive object images.

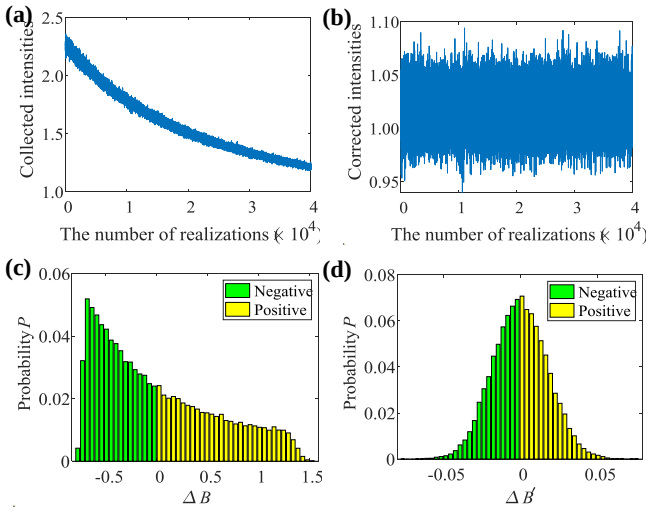

Fig. 3. (a) The directly collected single-pixel intensities corresponding to USAF 1951 resolution target, (b) temporally-corrected single-pixel intensities corresponding to USAF 1951 resolution target, (c) probability distribution of the directly collected single-pixel intensities corresponding to (a), and (d) probability distribution of the temporally-corrected single-pixel intensities corresponding to (b).

When the directly collected single-pixel intensities in Fig. 3(a) are used to recover object, experimental results are shown in Figs. 4(a)–4(c). Figure 4(a) shows a retrieved positive image, and Fig. 4(b) shows a retrieved negative image. Figure 4(c) shows a final correspondence image (i.e., positive image – negative image) using conventional correspondence imaging method. As can be seen in Figs. 4(a)–4(c), no information about USAF 1951 resolution target can be observed, which means that conventional correspondence imaging (i.e., directly sorting method) cannot reconstruct the object when imaging through complex scattering media is conducted. When the proposed correspondence imaging is applied, temporally-corrected single-pixel intensities can be obtained to identify effective illumination patterns that can be used to respectively retrieve high-quality positive and negative images. Figures 4(d)–4(f) show the retrieved object images, when temporally-corrected single-pixel intensities in Fig. 3(b) are applied. Figure 4(d) shows a retrieved positive image, and Fig. 4(e) shows a retrieved negative image. Figure 4(f) shows a final correspondence image (i.e., positive image – negative image) using the proposed correspondence imaging. As can be seen in Figs. 4(d)–4(f), high-quality

object information about USAF 1951 resolution target can be retrieved, which means that the proposed correspondence imaging effectively works through complex scattering media. In the proposed correpondence imaging, spatial resolution of 70.15 μm (i.e., element 6 of group 2 in USAF 1951 resolution target) is fully achieved in complex and dynamic scattering environment. With a calculation of the autocorrelation [54], theoretical resolution limit of the designed optical system is 40.0 μm.

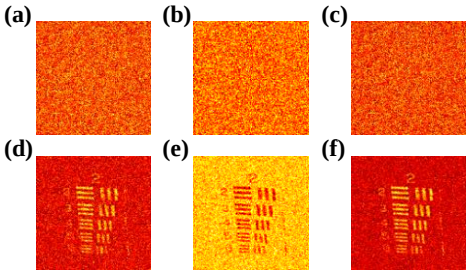

Fig. 4. (a) A positive image obtained by using conventional correspondence imaging through complex scattering media, (b) a negative image obtained by using conventional correspondence imaging through complex scattering media, (c) a final correspondence image using conventional correspondence imaging through complex scattering media, (d) a positive image obtained by using the proposed correspondence imaging through complex scattering media, (e) a negative image obtained by using the proposed correspondence imaging through complex scattering media, and (f) a final correspondence image using the proposed correspondence imaging through complex scattering media.

3.3. Imaging different objects

To illustrate robustness of the proposed correspondence imaging through complex scattering media, three different objects (i.e., object 1 “thumb”, object 2 “apple”, object 3 “flower”) are further tested based on the experimental setup in Fig. 2. A series of random illumination patterns are used to respectively illuminate three objects through turbid and dynamic water as shown in Fig. 2. The actual size of object 1, object 2 and object 3 is 7 mm (L) × 8 mm (W), 7 mm × 8 mm and 7 mm × 6 mm, respectively. The directly collected single-pixel intensity values corresponding to the three objects are shown in Figs. 5(a), 5(c) and 5(e), respectively. As shown in Figs. 5(a), 5(c) and 5(e), the directly collected single-pixel intensity values decrease as milk keeps dropping into the dynamic water tank in the imaging process. In a dynamic and turbid water environment, the directly collected single-pixel intensity values could be physically meaningless in conventional correspondence imaging, and cannot be applied for object retrieval. Hence, temporally correcting the directly collected single-pixel intensity values is significant. In the proposed method, it has been demonstrated that effective single-pixel intensities can be obtained after the temporally-corrected patterns are used, and the temporally-corrected single-pixel intensities are shown in Figs. 5(b), 5(d) and 5(f). The experimental results in Figs. 5(b), 5(d) and 5(f) demonstrate that the proposed method can effectively eliminate the effect of dynamic scaling factors in a complex and dynamic scattering environment.

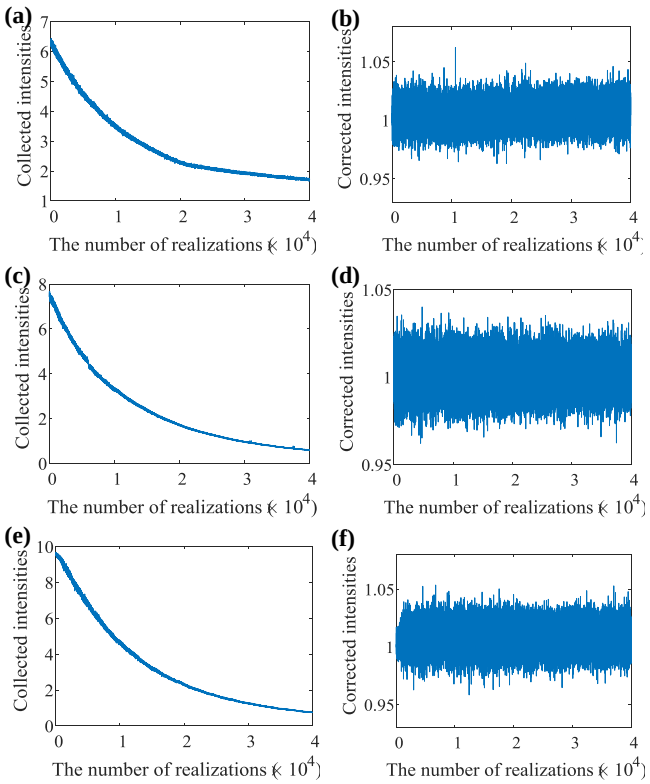

Fig. 5. (a), (c) and (e) The directly collected single-pixel intensities respectively corresponding to object 1, object 2 and object 3, and (b), (d) and (f) temporally-corrected single-pixel intensities respectively corresponding to object 1, object 2 and object 3.

Probability distribution of the recorded single-pixel intensities corresponding to object 1, object 2 and object 3 are further analyzed. The directly collected single-pixel intensities through complex scattering media do not satisfy the property of Gaussian distribution, as shown in Figs. 6(a), 6(c) and 6(e). Figures 6(a), 6(c) and 6(e) show probability distributions of the directly collected single-pixel intensities corresponding to object 1, object 2 and object 3, respectively. The results in Figs. 6(a), 6(c) and 6(e) are obtained based on the data in Figs. 5(a), 5(c) and 5(e), respectively. When temporal correction in the proposed correspondence imaging is used, the probability

distribution of temporally-corrected single-pixel intensities can be considered as Gaussian distribution, as shown in Figs. 6(b), 6(d) and 6(f). Figures 6(b), 6(d) and 6(f) show probability distribution of temporally-corrected single-pixel intensities corresponding to object 1, object 2 and object 3, respectively. The results in Figs. 6(b), 6(d) and 6(f) are obtained based on the data in Figs. 5(b), 5(d) and 5(f), respectively. The negative and positive legends in Fig. 6 mean that the corresponding single-pixel intensity values can be applied to further identify illumination patterns for retrieving negative and positive object images. The results in Fig. 6 also demonstrate powerful capability of the proposed correspondence imaging through complex and dynamic scattering media.

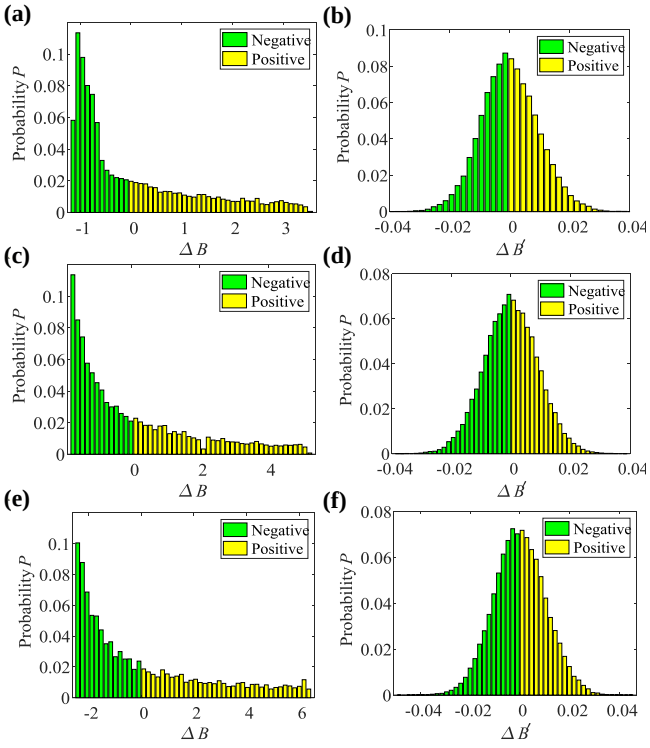

Fig. 6. (a), (c) and (e) Probability distribution of the directly collected single-pixel intensities respectively corresponding to object 1, object 2 and object 3, and (b), (d) and (f) probability distribution of the temporally-corrected single-pixel intensities respectively corresponding to object 1, object 2 and object 3.

To illustrate the proposed correspondence imaging through complex scattering media, positive and negative images are retrieved respectively based on the directly collected single-pixel intensities and temporally-corrected single-pixel intensities. Positive images can be retrieved by averaging the identified illumination patterns corresponding to the single-pixel intensity values which are larger than the mean intensity value. Negative images can be retrieved by averaging the identified illumination patterns corresponding to the single-pixel intensity values which are smaller than the mean value. For imaging each object, 40000 illumination patterns are used in optical experiments. According to the developed principles related to positive imaging, 14557, 14990 and 14922 illumination patterns are identified and respectively used for recovering object 1, object 2 and object 3, when conventional correspondence imaging (i.e., directly sorting method) is used. The retrieved positive images corresponding to object 1, object 2 and object 3 are shown in Figs. 7(a), 7(e), and 7(i), respectively. According to the developed principles related to negative imaging, 25443, 25010 and 25078 illumination patterns are identified and respectively used for recovering object 1, object 2 and object 3, when conventional correspondence imaging is used. The retrieved negative images are shown in Figs. 7(b), 7(f), and 7(j), respectively. As can be seen in Figs. 7(a), 7(b), 7(e), 7(f), 7(i) and 7(j), it is illustrated that conventional correspondence imaging is not effective, when imaging through complex scattering media is conducted. When the proposed correspondence imaging through complex scattering media is applied, positive and negative images can be retrieved with high quality, as shown in Figs. 7(c), 7(d), 7(g), 7(h), 7(k) and 7(l). For the retrieved positive images in Figs. 7(c), 7(g)

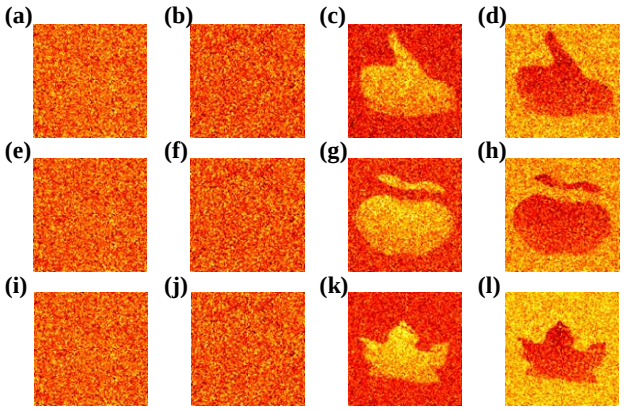

Fig. 7. (a), (e) and (i) The retrieved positive images using conventional correspondence imaging respectively corresponding to object 1, object 2 and object 3, (b), (f) and (j) the retrieved negative images using conventional correspondence imaging respectively corresponding to object 1, object 2 and object 3, (c), (g), and (k) the retrieved positive images using the proposed method respectively corresponding to object 1, object 2 and object 3, and (d), (h) and (l) the retrieved negative images using the proposed method respectively corresponding to object 1, object 2 and object 3.

and 7(k), the number of identified illumination patterns is 19506, 19905 and 19816, respectively. For the retrieved negative images in Figs. 7(d), 7(h) and 7(l), the number of identified illumination patterns is 20494, 20095 and 20184, respectively. When the proposed method is applied, the number of illumination patterns identified to retrieve positive images is approximately equal to that identified to retrieve negative images. The experimental results in Fig. 7 demonstrate effectiveness of the proposed correspondence imaging through complex and dynamic scattering media.

3.4. Comparisons among different methods

Comparisons among different methods, i.e., the proposed correspondence imaging, conventional correspondence imaging, conventional ghost imaging (GI) [16,17], differential ghost imaging (DGI) [27] and normalized ghost imaging (NGI) [28], are conducted. The method for GI can be described by

$$GI = \frac{1}{N}\sum\left(I_i - \langle I_i \rangle\right)\left(B_i - \langle B_i \rangle\right), \tag{19}$$

where $\langle\cdot\rangle$ denotes an ensemble average over N measurements.

The method for DGI can be described by

$$DGI = \frac{1}{N}\sum\left(I_i - \langle I_i \rangle\right)\left(B_i - \frac{\langle B_i \rangle}{\langle R_i \rangle}R_i\right), \tag{20}$$

where R_i denotes the total intensity of pattern I_i.

The method for NGI can be described by

$$NGI = \frac{1}{N}\sum\left(I_i - \langle I_i \rangle\right)\left(\frac{B_i}{R_i} - \frac{\langle B_i \rangle}{\langle R_i \rangle}\right). \tag{21}$$

Experimental results obtained by using these approaches are shown in Fig. 8. Using the proposed correspondence imaging, experimental results corresponding to object 1, object 2 and object 3 are shown in Figs. 8(a)–8(c), respectively. Figures 8(a)–8(c) show the finally reconstructed correspondence images, i.e., positive image – negative image. As seen in Figs. 8(a)–8(c), the proposed correspondence imaging can be used to recover high-quality objects, when there is a complex scattering medium. In contrast, conventional correspondence imaging cannot retrieve any object, as shown in Figs. 8(d)–8(f). Figures 8(d)–8(f) show the finally retrieved correspondence images respectively corresponding to object 1, object 2 and object 3 using conventional correspondence imaging. When conventional GI is applied with the directly collected single-pixel intensities, no information about the three objects can be reconstructed, as shown in Figs. 8(g)–8(i). The DGI and NGI methods [27,28] were developed to enhance quality of recovered objects. However, in a complex scattering environment, the DGI and NGI methods also cannot work. Experimental results corresponding to object 1, object 2 and object 3 using the DGI are shown in Figs. 8(j)–8(l). It can be seen in Figs. 8(j)–8(l) that no object can be observed. Experimental results obtained by using the NGI are shown in Figs. 8(m)–8(o). It can also be seen in Figs. 8(m)–8(o) that no object is observed. Based on experimental results in Fig. 8, it is demonstrated that conventional methods cannot work when a complex scattering medium is studied, and the proposed correspondence imaging is feasible and effective in retrieving high-quality object images.

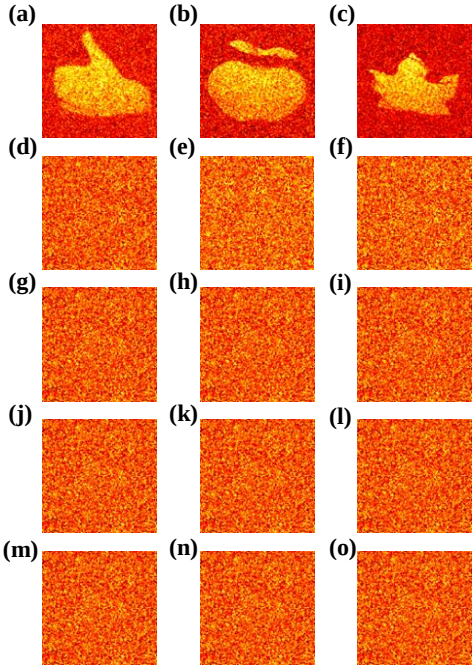

Fig. 8. (a)-(c) The experimental results obtained by using the proposed correspondence imaging respectively corresponding to object 1, object 2 and object 3, (d)-(f) experimental results obtained by using conventional correspondence imaging respectively corresponding to object 1, object 2 and object 3, (g)-(i) experimental results obtained by using conventional GI respectively corresponding to object 1, object 2 and object 3, (j)-(l) experimental results obtained by using the DGI respectively corresponding to object 1, object 2 and object 3, and (m)-(o) experimental results obtained by using the NGI respectively corresponding to object 1, object 2 and object 3.

Experimental results with the different number of realizations are further presented. In conventional methods, no information can be retrieved even with a large number of realizations in complex environments. Hence, the

experimental results using the proposed method are presented with the different number of realizations. When complex environment in Fig. 2 is applied, experimental results obtained by using the proposed method with the different number of realizations are shown in Fig. 9. When the proposed method with 10000 realizations is used, experimental results are shown in Figs. 9(a), 9(d) and 9(g). Figures 9(b), 9(e) and 9(h) show the retrieved final correspondence images using the proposed method with 20000 realizations corresponding to object 1, object 2 and object 3, respectively. When the proposed method with 30000 realizations is used, experimental results are shown in Figs. 9(c), 9(f) and 9(i). As can be seen in Fig. 9, quality of reconstructed objects can be guaranteed by using the proposed method through complex scattering media with the different number of realizations.

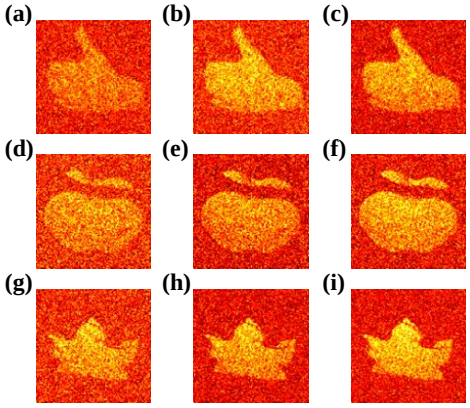

Fig. 9. (a), (d) and (g) The recovered images using the proposed method with 10000 realizations respectively corresponding to object 1, object 2 and object 3, (b), (e) and (h) the recovered images using the proposed method with 20000 realizations respectively corresponding to object 1, object 2 and object 3, and (c), (f), and (i) the recovered images using the proposed method with 30000 realizations respectively corresponding to object 1, object 2 and object 3.

3.5. Quality evaluation

The reconstructed objects are evaluated by using SNR defined by [55–61]

$$\mathrm{SNR} = \frac{\langle A_f \rangle - \langle A_b \rangle}{(\sigma_f + \sigma_b)/2}, \tag{22}$$

where $<A_f>$ and $<A_b>$ respectively denote average intensity of feature part and background part in the retrieved object image, and σ_f and σ_b respectively denote standard deviation of feature part and background part. The evaluation results corresponding to Fig. 8 are given in Table 1. In Table 1, Ours denotes experimental results obtained by using the proposed correspondence imaging, and CI denotes experimental results obtained by using conventional correspondence imaging. As can be found in Table 1, the proposed correspondence imaging always produces the best experimental results compared with other methods. The calculated SNR values demonstrate that the proposed correspondence imaging is feasible and effective to realize high-quality object reconstruction in complex and dynamic scattering media. In a highly dynamic scattering environment, scaling factors cannot be simply considered to be the same. The dynamic scaling factors severely affect the performance of conventional methods. The temporal carrier introduced in the proposed method can significantly reduce the effect of dynamic scattering factors in complex environments, and high-quality object reconstruction can be realized in complex scattering environments.

Table 1
SNR values of reconstructed objects in Fig. 8

	Object 1	Object 2	Object 3
Ours	**2.90**	**2.46**	**3.13**
CI	0.03	0.03	0.05
GI	0.11	0.07	0.09
DGI	0.11	0.07	0.09
NGI	0.11	0.07	0.09

3.6. SNR versus the number of realizations

Figure 10 shows a relationship between the number of realizations and SNR values of the reconstructed objects (i.e., object 1, object 2 and object 3 in Fig. 8) in conventional correspondence imaging, conventional GI and the proposed correspondence imaging. Figures 10(a), 10(c) and 10(e) show a comparison between the proposed method and conventional correspondence imaging for object 1, object 2 and object 3, respectively. As can be seen in Figs. 10(a), 10(c) and 10(e), SNR values of the reconstructed object 1, object 2 and object 3 in the proposed method increase correspondingly as the number of realizations increases, and SNR values of the three reconstructed objects can achieve up to 2.90, 2.46 and 3.13, respectively. However, SNR values of the reconstructed object 1, object 2 and object 3 in conventional correspondence imaging are always close to 0 even with a large number of realizations. Figures 10(b), 10(d) and 10(f) show a comparison between the proposed method and conventional GI for object 1, object 2 and object 3, respectively. As can be seen in Figs. 10(b), 10(d) and 10(f), SNR values of the reconstructed object 1, object 2 and object 3 in conventional GI are

always close to 0 even with a large number of realizations. It is experimentally demonstrated that the proposed correspondence imaging can effectively remove the effect of dynamic scaling factors via a temporal correction.

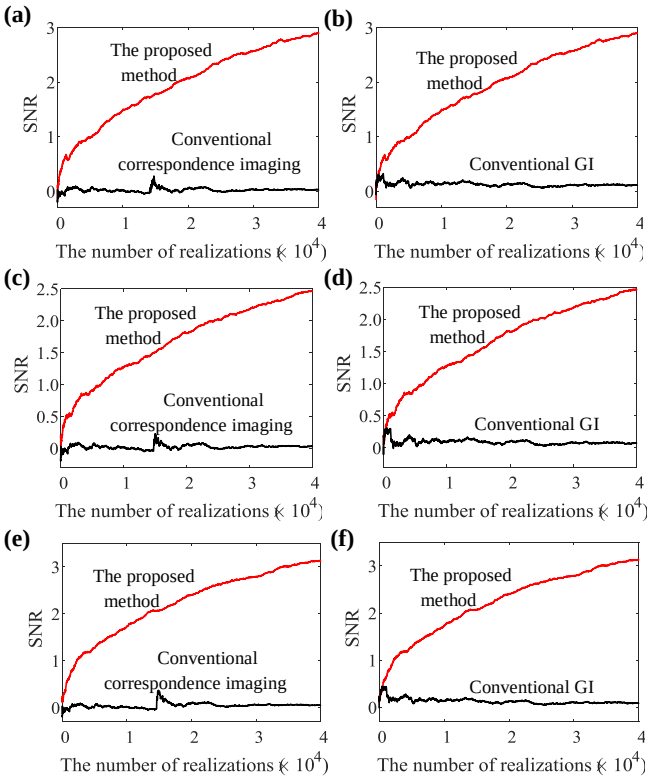

Fig. 10. Conventional correspondence imaging and the proposed method: the relationships between the different number of realizations and SNR values of the reconstructed (a) object 1, (c) object 2 and (e) object 3. Conventional GI and the proposed method: the relationships between the different number of realizations and SNR values of the reconstructed (b) object 1, (d) object 2 and (f) object 3.

The DGI [27] and NGI [28] were previously developed to enhance quality of the reconstructed objects, and SNR values based on these two methods are also calculated to evaluate quality of the reconstructed object 1, object 2 and object 3 when complex scattering medium is applied. Figures 11(a), 11(c) and 11(e) show SNR values of the reconstructed object 1, object 2 and object 3 obtained with the different number of realizations, when the DGI is used. Figures 11(b), 11(d) and 11(f) show SNR values of the reconstructed object 1, object 2 and object 3 obtained with the different number of realizations, when the NGI is used. It can be seen in Fig. 11 that SNR values of the reconstructed objects in the DGI and NGI are always close to 0. Experimental results in Fig. 11 are similar to those obtained by using conventional correspondence imaging and conventional GI in Fig. 10. The SNR values given in Fig. 11 further demonstrate advantages of the proposed method.

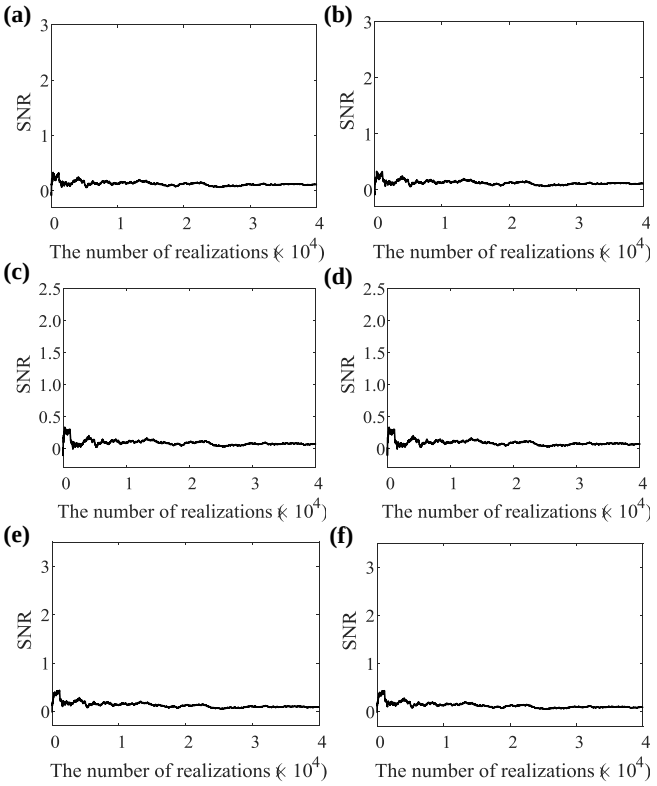

Fig. 11. (a), (c) and (e) SNR versus the different number of realizations in the DGI respectively for object 1, object 2 and object 3, (b), (d) and (f) SNR versus the different number of realizations in the NGI respectively for object 1, object 2 and object 3.

3.7. A basis for further enhancement

The proposed correspondence imaging can effectively solve the problems in conventional correspondence imaging, and can be flexibly used with other methods [34–40] to further enhance quality of the reconstructed objects. Here, as a typical example, we simply select two algorithms to further illustrate the flexibility. The proposed correspondence imaging with logarithm can be described by

$$R_{\log}(\mathbf{x}) = \frac{1}{N}\sum_{i=1}^{N}\left(\log_{\lambda}\frac{B_i'}{\mu'}\right)I_i(\mathbf{x}), \qquad (23)$$

where $R_{\log}(\mathbf{x})$ denotes the retrieved positive or negative image, and λ denotes a base of logarithmic function. The parameter λ is used to control the realization of positive or negative imaging. When λ is larger than 1.0, Eq. (23) is

used to retrieve a positive image. When λ is smaller than 1.0, Eq. (23) is used to retrieve a negative image. It was demonstrated [37] that conventional correspondence imaging with logarithm can achieve the higher quality in object reconstruction than conventional correspondence imaging in static scattering environments. When complex environment in Fig. 2 is applied, experimental results obtained by using conventional correspondence imaging with logarithm are shown in Figs. 12(a)–12(c), 12(g)–12(i) and 12(m)–12(o). Figures 12(a), 12(g) and 12(m) show the reconstructed positive images using conventional correspondence imaging with logarithm corresponding to object 1, object 2 and object 3, respectively. Figures 12(b), 12(h) and 12(n) show the retrieved negative images using conventional correspondence imaging with logarithm corresponding to object 1, object 2 and object 3, respectively. Figures 12(c), 12(i) and 12(o) show the final correspondence images using conventional correspondence imaging with logarithm corresponding to object 1, object 2 and object 3, respectively. As can be seen in Figs. 12(a)–12(c), 12(g)–12(i) and 12(m)–12(o), no object can be observed using conventional correspondence imaging with logarithm through complex scattering media. When the proposed method is applied with logarithm, the objects can be reconstructed with high quality. When the proposed method with logarithm is used, experimental results are shown in Figs. 12(d)–12(f), 12(j)–12(l) and 12(p)–12(r). Figures 12(d), 12(j) and 12(p) show the retrieved positive images using the proposed method with logarithm corresponding to object 1, object 2 and object 3, respectively. Figures 12(e), 12(k) and 12(q) show the retrieved negative images using the proposed method with logarithm corresponding to object 1, object 2 and object 3, respectively. Figures 12(f), 12(l) and 12(r) show the final correspondence images using the proposed method with logarithm corresponding to object 1, object 2 and object 3, respectively. Figures 12(s), 12(t) and 12(u) show the final correspondence images using the proposed method without logarithm corresponding to object 1, object 2 and object 3, respectively. As can be seen in Figs. 12(d)–12(f), 12(j)–12(l) and 12(p)–12(r), high-quality objects can be reconstructed by using the proposed method with logarithm through complex scattering media. Experimental results in Fig. 12 demonstrate that the proposed method can provide a basis to be used with other methods to further enhance reconstruction quality.

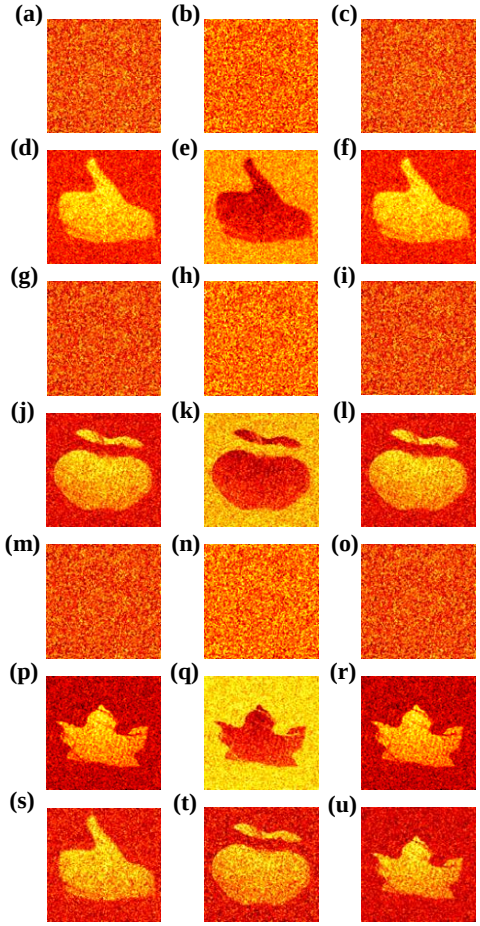

Fig. 12. (a), (g) and (m) The retrieved positive images using conventional correspondence imaging with logarithm respectively corresponding to object 1, object 2 and object 3, (b), (h) and (n) the retrieved negative images using conventional correspondence imaging with logarithm respectively corresponding to object 1, object 2 and object 3, (c), (i), and (o) the retrieved final correspondence images using conventional correspondence imaging with logarithm respectively corresponding to object 1, object 2 and object 3, (d), (j) and (p) the retrieved positive images using the proposed method with logarithm respectively corresponding to object 1, object 2 and object 3, (e), (k) and (q) the retrieved negative images using the proposed method with logarithm respectively corresponding to object 1, object 2 and object 3, (f), (l), and (r) the retrieved final correspondence images using the proposed method with logarithm respectively corresponding to object 1, object 2 and object 3, and (s), (t), and (u) the retrieved final correspondence images using the proposed method without logarithm respectively corresponding to object 1, object 2 and object 3.

Figure 13 shows the relationships between the number of realizations and SNR values of the reconstructed objects (i.e., object 1, object 2 and object 3) in conventional correspondence imaging with logarithm, the proposed method with logarithm and the proposed method. Figures 13(a), 13(c) and 13(e) show a comparison between the

proposed method with logarithm and conventional correspondence imaging with logarithm for object 1, object 2 and object 3, respectively. As can be seen in Figs. 13(a), 13(c) and 13(e), SNR values of the reconstructed object 1, object 2 and object 3 in the proposed method with logarithm increase correspondingly as the number of realizations increases. SNR values of the reconstructed object 1, object 2 and object 3 in conventional correspondence imaging with logarithm are always close to 0 even with a large number of realizations. Figures 13(b), 13(d) and 13(f) show a comparison between the proposed correspondence imaging method with logarithm and the proposed correspondence imaging method for object 1, object 2 and object 3, respectively. As can be seen in Figs. 13(b), 13(d) and 13(f), SNR values of the reconstructed object 1, object 2 and object 3 in the proposed method with logarithm are always higher than those obtained in the proposed correspondence imaging.

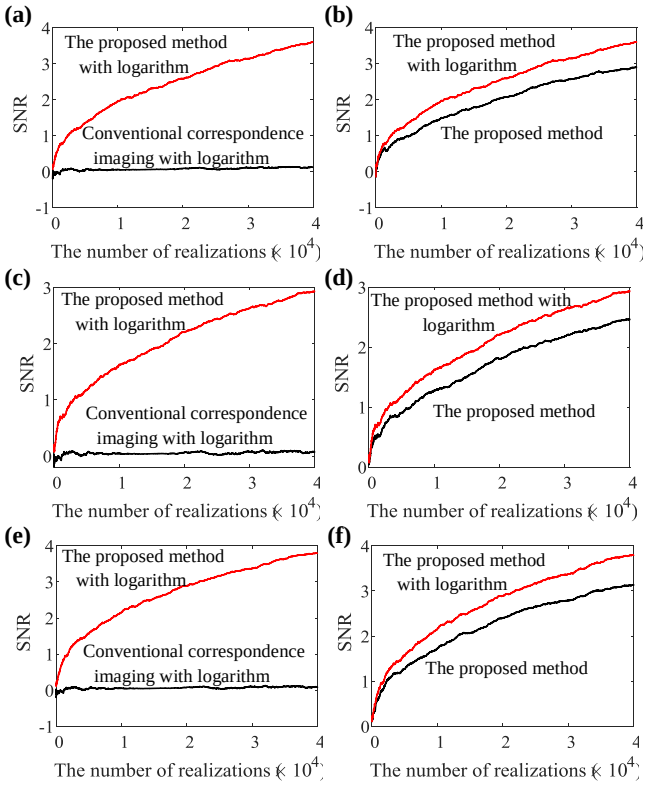

Fig. 13. Conventional correspondence imaging with logarithm and the proposed method with logarithm through complex scattering media: the relationships between the different number of realizations and SNR values of the reconstructed (a) object 1, (c) object 2 and (e) object 3. The proposed method with logarithm and the proposed method: the relationships between the different number of realizations and SNR values of the reconstructed (b) object 1, (d) object 2 and (f) object 3.

Another existing method is correspondence imaging with exponential, which is described by [37]

$$R_e(\mathbf{x}) = \frac{1}{N}\sum_{i=1}^{N} \tau^{CB_i' \Big/ \sum_{\mathbf{x}} I_i(\mathbf{x})} I_i(\mathbf{x}), \qquad (24)$$

where $R_e(\mathbf{x})$ denotes a reconstructed positive or negative image, τ denotes a base of exponential function, and C denotes a constant. It was demonstrated [37] that correspondence imaging with exponential is more powerful compared with basic correspondence imaging. In Eq. (24), when τ^C is larger than 1, positive imaging can be realized. When τ^C is smaller than 1, negative imaging can be realized.

When the complex environment in Fig. 2 is applied, experimental results obtained by using conventional correspondence imaging with exponential are shown in Figs. 14(a)–14(c), 14(g)–14(i) and 14(m)–14(o). Figures 14(a), 14(g) and 14(m) show the reconstructed positive images using conventional correspondence imaging with exponential corresponding to object 1, object 2 and object 3, respectively. Figures 14(b), 14(h) and 14(n) show the retrieved negative images using conventional correspondence imaging with exponential corresponding to object 1, object 2 and object 3, respectively. Figures 14(c), 14(i) and 14(o) show the final correspondence images using conventional correspondence imaging with exponential corresponding to object 1, object 2 and object 3, respectively. As can be seen in Figs. 14(a)–14(c), 14(g)–14(i) and 14(m)–14(o), no object can be observed using conventional correspondence imaging with exponential through complex scattering media. When the proposed method is applied with exponential, the objects can be reconstructed with high quality. When the proposed method with exponential is used, experimental results are shown in Figs. 14(d)–14(f), 14(j)–14(l) and 14(p)–14(r). Figures 14(d), 14(j) and 14(p) show the retrieved positive images using the proposed method with exponential corresponding to object 1, object 2 and object 3, respectively. Figures 14(e), 14(k) and 14(q) show the retrieved negative images using the proposed method with exponential corresponding to object 1, object 2 and object 3, respectively. Figures 14(f), 14(l) and 14(r) show the final correspondence images using the proposed method with exponential corresponding to object 1, object 2 and object 3, respectively. As can be seen in Figs. 14(d)–14(f), 14(j)–14(l) and 14(p)–14(r), high-quality objects can be reconstructed by using the proposed method with exponential through complex scattering media. Experimental results in Fig. 14 demonstrate that the proposed method can provide a basis to be used with other

methods to further enhance reconstruction quality. It can be expected that untrained neural networks can also be further applied.

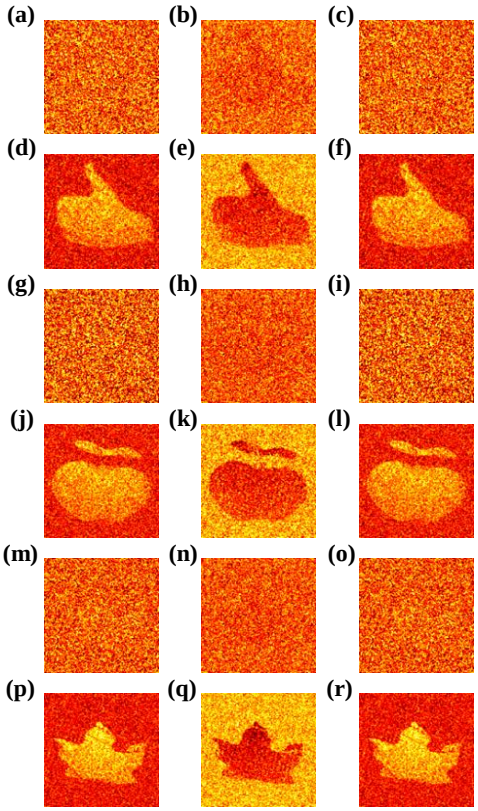

Fig. 14. (a), (g) and (m) The retrieved positive images using conventional correspondence imaging with exponential respectively corresponding to object 1, object 2 and object 3, (b), (h) and (n) the retrieved negative images using conventional correspondence imaging with exponential respectively corresponding to object 1, object 2 and object 3, (c), (i), and (o) the retrieved final correspondence images using conventional correspondence imaging with exponential respectively corresponding to object 1, object 2 and object 3, (d), (j) and (p) the retrieved positive images using the proposed method with exponential respectively corresponding to object 1, object 2 and object 3, (e), (k) and (q) the retrieved negative images using the proposed method with exponential respectively corresponding to object 1, object 2 and object 3, (f), (l), and (r) the retrieved final correspondence images using the proposed method with exponential respectively corresponding to object 1, object 2 and object 3.

4. Conclusions

We have reported a correspondence imaging approach to reconstructing high-quality objects through complex scattering media where conventional methods cannot work. Optical channel characteristics, i.e., dynamic scaling factors, have been studied in complex scattering environments, and temporally-corrected patterns are introduced to eliminate the effect of dynamic scaling factors in the proposed correspondence imaging. A rectified theory has been developed to complete the formation mechanism of correspondence imaging through complex scattering media. A series of optical experiments have been conducted to verify the proposed method and fully compare it with conventional methods. Experimental results demonstrate that the proposed correspondence imaging provides a powerful tool to reconstruct objects through complex scattering media. It could be believed that the proposed method could provide a new insight into correspondence imaging through complex scattering media with single-pixel measurements for high-quality object reconstruction. The principle proposed in this study can also be combined with other imaging techniques to improve the imaging performance in various scattering environments.

CRediT authorship contribution statement

Yin Xiao: Conceptualization, Validation, Investigation, Visualization, Data curation, Formal analysis, Methodology, Writing – original draft, Writing – review & editing. **Lina Zhou:** Writing – review & editing. **Wen Chen:** Conceptualization, Supervision, Funding acquisition, Project administration, Formal analysis, Methodology, Writing – review & editing.

Acknowledgments

This work was supported by Hong Kong Research Grants Council (C5011-19G, 15224921, 15223522), Basic and Applied Basic Research Foundation of GuangDong Province (2023A1515010831, 2022A1515011858) and The Hong Kong Polytechnic University (1-W19E, 1-BD4Q, 1-WZ4M).

Declaration of Competing Interest

All authors declare that no conflict of interest exists.

Data availability

Data will be made available on request.

References

[1] C. Yang, D. Qi, F. Cao, Y. He, J. Yao, P. Ding, X. Ouyang, Y. Yu, T. Jia, S. Xu, Z. Sun, and S. Zhang, Single-shot receive-only ultrafast electro-optical deflection imaging, Phys. Rev. Appl. **13**, 024001 (2020).

[2] D. Qi, C. Yang, F. Cao, J. Liang, Y. He, Y. Yang, T. Jia, Z. Sun, and S. Zhang, Compressed ultrafast electron diffraction imaging through electronic encoding, Phys. Rev. Appl. **10**, 054061 (2018).

[3] Y. Guo, H. Han, L. Wang, Y. Zhu, X. Gao, Z. Yang, X. Weng, W. Yan, and J. Qu, Label free deep penetration single photon microscopic imaging with ultralong anti-diffracting beam, Appl. Phys. Lett. **121**, 023701 (2022).

[4] V. Ntziachristos, Going deeper than microscopy: the optical imaging frontier in biology, Nat. Methods **7**, 603 (2010).

[5] I. Vellekoop and A. Mosk, Focusing coherent light through opaque strongly scattering media, Opt. Lett. **32**, 2309 (2007).

[6] A. P. Mosk, A. Lagendijk, G. Lerosey, and M. Fink, Controlling waves in space and time for imaging and focusing in complex media, Nat. Photonics **6**, 283 (2012).

[7] S. Rotter and S. Gigan, Light fields in complex media: mesoscopic scattering meets wave control, Rev. Mod. Phys. **89**, 015005 (2017).

[8] E. Bettelheim, N. R. Smith, and B. Meerson, Inverse scattering method solves the problem of full statistics of nonstationary heat transfer in the Kipnis-Marchioro-Presutti model, Phys. Rev. Lett. **128**, 130602 (2022).

[9] X. D. Chen, Computational Methods for Electromagnetic Inverse Scattering, Wiley-IEEE, 2018.

[10] A. Krajenbrink and P. L. Doussal, Inverse scattering solution of the weak noise theory of the Kardar-Parisi-Zhang equation with flat and Brownian initial conditions, Phys. Rev. E **105**, 054142 (2022).

[11] J. W. Goodman, Speckle Phenomena in Optics: Theory and Applications, (Roberts & Company, 2007).

[12] S. Popoff, G. Lerosey, R. Carminati, M. Fink, A. Boccara, and S. Gigan, Measuring the transmission matrix in optics: an approach to the study and control of light propagation in disordered media, Phys. Rev. Lett. **104**, 100601 (2010).

[13] M. Kim, W. Choi, Y. Choi, C. Yoon, and W. Choi, Transmission matrix of a scattering medium and its applications in biophotonics, Opt. Express, **23**, 12648 (2015).

[14] H. Liu, Y. Chen, L. Zhang, D. Li, and X. W. Li, Color ghost imaging through the scattering media based on A-cGAN, Opt. Lett. **47**, 569 (2022).

[15] Y. Liao, H. Liu, S. K. Kim, and X. W. Li, Optical steganography with RVNCA-based keys for 3D object, Opt. Lasers Eng. **169**, 107740 (2023).

[16] D. V. Strekalov, A. V. Sergienko, D. N. Klyshko, and Y. H. Shih, Observation of two-photon 'ghost' interference and diffraction, Phys. Rev. Lett. **74**, 3600 (1995).

[17] R. S. Bennink, S. J. Bentley, and R. W. Boyd, "Two-photon" coincidence imaging with a classical source, Phys. Rev. Lett. **89**, 113601 (2002).

[18] B. Sun, M. P. Edgar, R. Bowman, L. E. Vittert, S. Welsh, A. Bowman, and M. J. Padgett, 3D computational imaging with single-pixel detectors, Science **340**, 844 (2013).

[19] A. Gatti, E. Brambilla, M. Bache, and L. A. Lugiato, Ghost imaging with thermal light: comparing entanglement and classical correlation, Phys. Rev. Lett. **93**, 093602 (2004).

[20] R. H. Hadfield, Single-photon detectors for optical quantum information applications, Nat. Photonics **3**, 696 (2009).

[21] D. Pelliccia, A. Rack, M. Scheel, V. Cantelli, and D. M. Paganin, Experimental X-ray ghost imaging, Phys. Rev. Lett. **117**, 113902 (2016).

[22] H. Yu, R. H. Lu, S. S. Han, H. L. Xie, G. H. Du, T. Q. Xiao, and D. M. Zhu, Fourier-transform ghost imaging with hard X rays, Phys. Rev. Lett. **117**, 113901 (2016).

[23] J. Greenberg, K. Krishnamurthy, and D. Brady, Compressive single-pixel snapshot x-ray diffraction imaging, Opt. Lett. **39**, 111 (2014).

[24] C. M. Watts, D. Shrekenhamer, J. Montoya, G. Lipworth, J. Hunt, T. Sleasman, S. Krishna, D. R. Smith, and Willie J. Padilla, Terahertz compressive imaging with metamaterial spatial light modulators, Nat. Photonics, **8**, 605 (2014).

[25] W. L. Chan, K. Charan, D. Takhar, K. F. Kelly, R. G. Baraniuk, and D. M. Mittleman, A single-pixel terahertz imaging system based on compressed sensing, Appl. Phys. Lett. **93**, 121105 (2008).

[26] R. I. Stantchev, B. Sun, S. M. Hornett, P. A. Hobson, G. M. Gibson, M. J. Padgett, and E. Hendry, Noninvasive, near-field terahertz imaging of hidden objects using a single-pixel detector, Sci. Adv. **2**, e1600190 (2016).

[27] F. Ferri, D. Magatti, L. A. Lugiato, and A. Gatti, Differential ghost imaging, Phys. Rev. Lett. **104**, 253603 (2010).

[28] B. Q. Sun, S. S. Welsh, M. P. Edgar, J. H. Shapiro, and M. J. Padgett, Normalized ghost imaging, Opt. Express, **20**, 16892 (2012).

[29] Z. Zhang, X. Ma, and J. Zhong, Single-pixel imaging by means of Fourier spectrum acquisition, Nat. Comm. **6**, 6225 (2015).

[30] L. Bian, J. Suo, X. Hu, F. Chen, and Q. Dai, Efficient single pixel imaging in Fourier space, J. Opt. **18**, 085704 (2016).

[31] B. L. Liu, Z. H. Yang, X. Liu and L. A. Wu, Coloured computational imaging with single-pixel detectors

based on a 2D discrete cosine transform, J. Mod. Opt. **64**, 259 (2016).
[32] Y. Xiao, L. Zhou, and W. Chen, Direct single-step measurement of Hadamard spectrum using single-pixel optical detection, IEEE Photon. Technol. Lett. **31**, 845 (2019).
[33] K. H. Luo, B. Q. Huang, W. M. Zheng, and L. A. Wu, Nonlocal imaging by conditional averaging of random reference measurements, Chin. Phys. Lett. **29**, 074216 (2012).
[34] M. F. Li, Y. R. Zhang, K. H. Luo, L. A. Wu, and H. Fan, Time-correspondence differential ghost imaging, Phys. Rev. A **87**, 033813 (2013).
[35] M. F. Li, Y. R. Zhang, X. F. Liu, X. R. Yao, K. H. Luo, H. Fan, and L. A. Wu, A double-threshold technique for fast time-correspondence imaging, Appl. Phys. Lett. **103**, 211119 (2013).
[36] H. Yang, S. Wu, H. B. Wang, D. Z. Cao, S. H. Zhang, J. Xiong, and K. Wang, Probability theory in conditional-averaging ghost imaging with thermal light, Phys. Rev. A **98**, 053853 (2018).
[37] H. C. Liu, H. Yang, J. Xiong, and S. Zhang, Positive and negative ghost imaging, Phys. Rev. Appl. **12**, 034019 (2019).
[38] Z. Ye, J. Xiong, and H. C. Liu, Ghost difference imaging using one single-pixel detector, Phys. Rev. Appl. **15**, 034035 (2021).
[39] J. Leng, W. K. Yu, and S. F. Wang, Formation mechanism of correspondence imaging with thermal light, Phys. Rev. A **101**, 033835 (2020).
[40] L. Y. Dou, L. Q. Ren, D. Z. Cao, and X. B. Song, Positive-negative ghost imaging with statistics of realizations, Phys. Rev. Appl. **16**, 044013 (2021).
[41] P. Zhang, W. Gong, X. Shen, and S. Han, Correlated imaging through atmospheric turbulence, Phys. Rev. A **82**, 033817 (2010).
[42] R. E. Meyers, K. S. Deacon, and Y. Shih, Turbulence-free ghost imaging, Appl. Phys. Lett. **98**, 111115 (2011).
[43] Z. Zhang, Z. Liu, and S. Liu, Expanding the memory effect in scattering imaging by manipulating photon distributions, Phys. Rev. A **106**, 043508 (2022).
[44] S. Liu, P. Li, H. Sha, J. Dong, Y. Huang, Y. Zhao, X. Yao, Q. Peng, X Li, X. Lin, and Y. Zhang, Intensity and phase imaging through scattering media via deep despeckle complex neural networks, Opt. Lasers Eng. **159**, 107196 (2022).
[45] H. Li, J. Shi, Y. Zhu, and G. Zeng, Periodic diffraction correlation imaging through strongly scattering mediums, Appl. Phys. Lett. **103**, 051901 (2013).
[46] W. Gong and S. Han, Correlated imaging in scattering media, Opt. Lett., **36**, 394 (2011).
[47] E. Tajahuerce, V. Durán, P. Clemente, E. Irles, F. Soldevila, P. Andrés, and J. Lancis, Image transmission through dynamic scattering media by single-pixel photodetection, Opt. Express **22**, 16945 (2014).
[48] V. Durán, F. Soldevila, E. Irles, P. Clemente, E. Tajahuerce, P. Andrés, and J. Lancis, Compressive imaging in scattering media, Opt. Express **23**, 14424 (2015).
[49] Y. Xiao, L. Zhou, and W. Chen, High-resolution ghost imaging through complex scattering media via a temporal correction, Opt. Lett. **47**, 3692 (2022).
[50] L. Wind and W. W. Szymanski, Quantification of scattering corrections to the Beer-Lambert law for transmittance measurements in turbid media, Meas. Sci. Technol. **13**, 270 (2002).
[51] R. Joshi, T. O'Connor, X. Shen, M. Wardlaw, and B. Javidi, Optical 4D signal detection in turbid water by multidimensional integral imaging using spatially distributed and temporally encoded multiple light sources, Opt. Express **28**, 10477 (2020).
[52] Z. L. Pan, Y. Xiao, Y. G. Cao, L. N. Zhou, and W. Chen, Optical data transmission through highly dynamic and turbid water using dynamic scaling factors and single-pixel detector, Opt. Express **30**, 43480 (2022).
[53] Z. L. Pan, Y. Xiao, Y. G. Cao, L. N. Zhou, and W. Chen, Optical analog-signal transmission and retrieval through turbid water, Appl. Opt. **60**, 10704 (2021).
[54] Y. Klein, O. Sefi, H. Schwartz, and S. Shwartz, Chemical element mapping by X-ray computational ghost fluorescence, Optica **9**, 63 (2022).
[55] B. Redding, M. A. Choma, and H. Cao, Speckle-free laser imaging using random laser illumination, Nat. Photonics **6**, 355 (2012).
[56] R. N. Bryan, Introduction to the Science of Medical Imaging (Cambridge University, 2009), Chap. 3, pp. 85–88.
[57] P. Zerom et al., Thermal ghost imaging with averaged speckle patterns, Phys. Rev. A **86**, 063817 (2012).
[58] L. Zhou, Y. Xiao, and W. Chen, Self-corrected orthonormalized ghost imaging through dynamic and complex scattering media, Appl. Phys. Lett. **123**, 011107 (2023).
[59] Y. Peng and W. Chen, Learning-based correction with Gaussian constraints for ghost imaging through dynamic scattering media, Opt. Lett. **48**, 4480-4483 (2023).
[60] L. Zhou, Y. Xiao, and W. Chen, High-resolution self-corrected single-pixel imaging through dynamic and complex scattering media, Opt. Express **31**, 23027–23039 (2023).
[61] L. Zhou, Y. Xiao, and W. Chen, Edge detection in gradient ghost imaging through complex media, Appl. Phys. Lett. **123**, 111104 (2023).